Spatiotemporal Mapping of a Photocurrent Vortex in Monolayer MoS₂ Using Diamond Quantum Sensors

Brian B. Zhou[1,2,*,†] Paul C. Jerger,[1,*] Kan-Heng Lee,[1,3] Masaya Fukami,[1] Fauzia Mujid[4]
Jiwoong Park,[1,4] and David D. Awschalom[1,5,‡]

[1]*Pritzker School of Molecular Engineering, University of Chicago, Chicago, Illinois 60637, USA*
[2]*Department of Physics, Boston College, Chestnut Hill, Massachusetts 02467, USA*
[3]*School of Applied and Engineering Physics, Cornell University, Ithaca, New York 14853, USA*
[4]*Department of Chemistry and James Franck Institute, University of Chicago,*
Chicago, Illinois 60637, USA
[5]*Center for Molecular Engineering and Materials Science Division, Argonne National Laboratory,*
Lemont, Illinois 60439, USA

Photocurrents are central to understanding and harnessing the interaction of light with matter. Here, we introduce a contact-free method to spatially resolve photocurrent distributions using proximal quantum magnetometers. We interface monolayer MoS₂ with a near-surface ensemble of nitrogen-vacancy centers in diamond and map the generated photothermal current distribution through its magnetic-field profile. By synchronizing pulsed photoexcitation with dynamical decoupling of the sensor spin, we extend the sensor's quantum coherence and resolve time-dependent, two-dimensional current densities as small as 20 nA/μm, with a projected sensitivity of 200 nA/(μm$\sqrt{\text{Hz}}$). Our spatially resolved measurements reveal that optical excitation can generate micron-sized photocurrent vortices in MoS₂, manifesting a photo-Nernst effect exceeding that of gate-tuned graphene at comparable magnetic fields. We further probe the rise time of the photocurrents and show that thermal diffusion determines its spatial variation. These spatiotemporal capabilities establish an optically accessed, local probe for optoelectronic phenomena, ideally suited to the emerging class of two-dimensional materials, for which making contacts is challenging and can alter the intrinsic material properties.

Subject Areas: Condensed Matter Physics,
Materials Science, Quantum Physics

I. INTRODUCTION

The extraordinary features of two-dimensional van der Waals systems have opened new directions for tailoring the interaction of light with matter, with the potential to impact technologies for imaging, communications, and energy harvesting. The detection of photo-induced carriers is critical to realizing practical photosensing and photovoltaic devices [1–3], as well as to characterizing novel photo-responses, including optical manipulation of spin and valley indices [4,5], circular [6–8] and shift [9,10] photo-currents driven by nontrivial Berry curvature, and scattering-protected photocurrents at a Dirac point [11]. Although

*These authors contributed equally to this work.
†brian.zhou@bc.edu
‡awsch@uchicago.edu

commonly used, transport-based detection of photocurrents cannot resolve the spatial distribution of current flow. Moreover, it is susceptible to inefficient photocarrier extraction, requiring light to be directed near junctions with a strong built-in electric field, which complicates the scale-up of devices to practical sizes [1–3]. To expand our understanding of light-matter interaction and overcome existing technical limitations, the detection of photocurrents with high spatio-temporal resolution and sensitivity is needed.

In this work, we introduce a novel technique using embedded quantum magnetometers [12–14] to probe the photocurrent response in 2D materials with submicron spatial resolution and submicrosecond temporal resolution. Here, we transfer a monolayer MoS₂ (1L-MoS₂) sheet grown by metal-organic chemical vapor deposition [15] (MOCVD) onto a diamond chip hosting a near-surface ensemble of nitrogen-vacancy (NV) centers. By measuring the NV center spin precession as a function of position, we map the local magnetic field generated by the photocurrents and deduce the distribution and direction of photocurrent flow. Remarkably, we find that photocurrents generated by the photothermoelectric effect (PTE) [16,17] in MoS₂
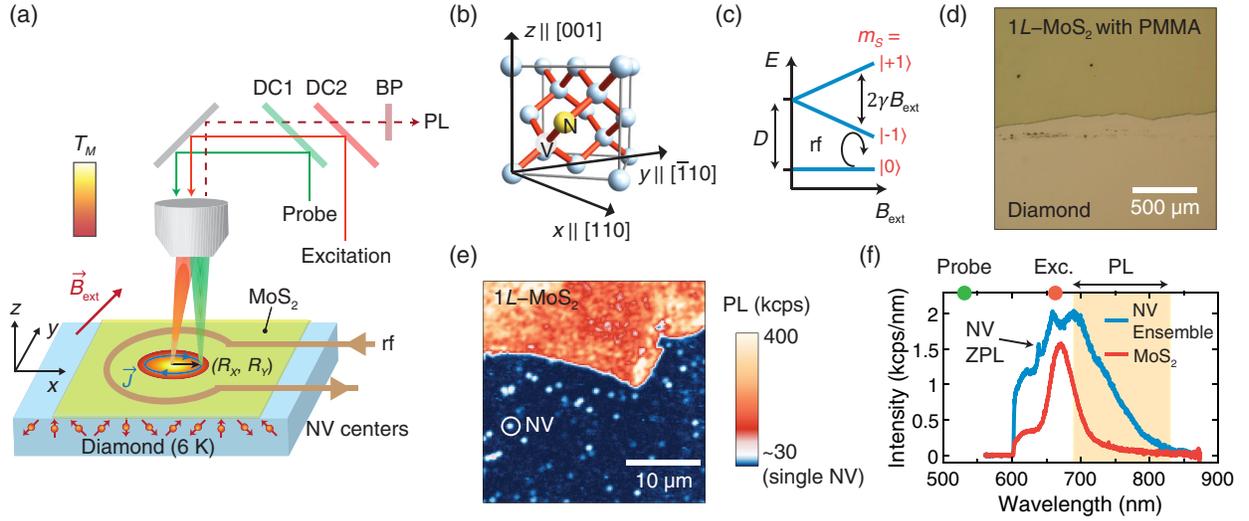
FIG. 1. Mapping photocurrents in monolayer MoS_2 with NV centers. (a) Experimental setup. A monolayer MoS_2 sheet is transferred onto a diamond sample hosting a near-surface ensemble of NV centers. An excitation laser (661 nm) generates a temperature distribution T_M within MoS_2 that drives a circulating photocurrent distribution $\vec{J}$. The NV center senses the local magnetic field produced by the photocurrents and is optically read out by a separate probe laser (532 nm). DC1/DC2—dichroic mirrors at 550/685 nm; BP—bandpass (690–830 nm). (b) NV center in the diamond lattice. We address the subset of NV centers aligned with the [111] direction. (c) Energy levels of the NV spin triplet as a function of B_{ext}, the magnetic field parallel to the NV axis. Resonant microwave pulses (rf) manipulate an equal superposition of the $m_s = |0\rangle$ and $|-1\rangle$ states for phase acquisition. D—zero-field splitting. (d) Optical micrograph of monolayer MoS_2 on diamond after vacuum transfer. To enhance optical contrast, this micrograph is taken prior to cleaning off a poly(methyl methacrylate) (PMMA) support layer. (e) Room-temperature PL image of the boundary between monolayer MoS_2 and bare diamond, containing single NV centers. (f) Room-temperature PL spectrum of monolayer MoS_2 and an ensemble NV sample under 532-nm illumination. The photoexcitation wavelength (661 nm) is longer than the NV zero-phonon line (ZPL; 637 nm) to minimize optical excitation of the NV center. The orange shaded region depicts the collected PL for NV spin readout.

circulate as vortices around the excitation spot under a small applied magnetic field, indicating a strong photo-Nernst effect [18,19]. Broadly speaking, our all-optical, near-field probe eliminates the need for electrical contacts and avoids the challenge of photocarrier extraction in large-area devices [2]. In contrast to scanning photocurrent microscopy [6–11,16], our technique provides diffraction-limited spatial resolution for both excitation and detection [Fig. 1(a)]. This capability extracts detailed spatial information even when the net photocurrent between two contacts in a conventional measurement is zero, as exemplified by the vortices probed here.

With wide phase-space applicability and potential nanoscale spatial resolution, NV magnetometry has emerged as a premier tool for probing current distributions in materials [13], revealing insights on the structure of vortices in high-T_c superconductors [20,21] and the effect of microscopic inhomogeneity on transport in graphene [22] and nanowires [23]. These demonstrations all probed direct current (dc) flow and were accordingly limited in sensitivity by the inhomogeneous dephasing time T_2^* of the NV center. Here, we leverage control over the photoexcitation timing to implement a "quantum lock-in" protocol [24–26] to detect time-dependent photocurrents. This protocol simultaneously decouples the NV center from wideband magnetic

noise, extending its coherence time to the homogeneous T_2 limit, and it achieves an estimated sensitivity to a 2D current density of 200 nA/(μm$\sqrt{Hz}$), approaching the sensitivity of superconducting quantum interference devices [27,28]. We resolve time-varying (ac) current densities as small as 20 nA/μm in MoS_2, 50 times smaller than the projected NV detection limit ($\sim$1 μA/μm) for dc currents in graphene [22]. Moreover, by changing the repetition rate of the photoexcitation pulses, we utilize our protocol to probe the nonequilibrium dynamics of photothermal carrier generation at submicrosecond timescales. Combining spatial and temporal resolution, we characterize the spatial dependence of the temporal response of PTE photocurrents in MoS_2, showing it to be driven by thermal diffusion.

II. HYBRID NV-MoS_2 PHOTOSENSING PLATFORM

Figure 1(a) displays the experimental setup for detecting photocurrents in monolayer MoS_2 by local magnetometry. Two independently steerable laser beams (probe at 532 nm and excitation at 661 nm) are joined by dichroic mirrors and focused by a confocal microscope onto the MoS_2-diamond stack, held at a base temperature of 6 K (see Supplemental

Material Sec. I [29]). The 532-nm probe beam initializes the NV center into the $m_s = |0\rangle$ sublevel and triggers spin-dependent photoluminescence (PL) that distinguishes $|0\rangle$ from $|\pm 1\rangle$ [13]. We define the coordinate axes $\{x, y, z\}$ to be parallel to the edges of the [001]-faced diamond sample with [110]-cut edges, as depicted in Fig. 1(b). The position of the probe spot relative to the excitation spot on the sample is denoted by the vector (R_x, R_y). By aligning the external magnetic field B_{ext} along the oblique [111] axis, we selectively address a single subset out of the four possible NV lattice orientations. An insulated wire coil placed over the MoS_2 monolayer delivers the resonant rf pulses for NV spin manipulation. Figure 1(c) shows the energy levels of the NV spin-triplet ground state, with the $|\pm 1\rangle$ sublevels separated from $|0\rangle$ by the zero-field splitting parameter $D = 2.87$ GHz. Applying B_{ext} along the NV center axis lifts the degeneracy of the $|\pm 1\rangle$ states, which acquire equal and opposite Zeeman shifts at a rate $\gamma = 2.8$ MHz/Gauss.

In Fig. 1(d), we display an optical micrograph of a MoS_2-diamond stack assembled by vacuum stacking [30] (see Appendix A for fabrication details and Supplemental Material Sec. II for atomic force microscope images [29]). The high-quality MOCVD-grown monolayer [15] initially covers our entire $2 \times 2 \times 0.5$-mm diamond sample, but we expose a portion of the diamond to perform control measurements. The slight absorption [31] of the 532-nm probe laser by the single atomic layer of MoS_2 does not interfere with initialization of the NV center spin state. However, monolayer MoS_2's strong intrinsic PL from 532-nm excitation partially overlaps the NV emission spectrum and overwhelms the signal of single NV centers covered by the monolayer [Fig. 1(e)]. To increase the NV signal and facilitate arbitrary spatial mapping, we instead utilize an engineered diamond sample hosting an ensemble of near-surface NV centers (about 40 nm deep, with about 85 NV centers per focused optical spot). Additionally, we band-pass filter the detected PL between 690 nm and 830 nm to predominantly isolate NV center emission, as shown in the room-temperature PL spectra of monolayer MoS_2 and a typical ensemble NV sample [Fig. 1(f)]. Importantly, the excitation wavelength for photocarriers in MoS_2 must be longer than the zero-phonon line of the NV center (637 nm) to minimize absorption [32] and subsequent decoherence [33] by the NV center during the photocurrent sensing duration. We excite at 661 nm, but we have verified that our effects persist for longer excitation wavelengths (see Supplemental Material Sec. V [29]).

Our photocurrent sensing protocol (see Appendix B) is based on the XY8-N dynamical decoupling sequence that enables frequency-selective detection of ac magnetic fields through the precession of the NV center spin [24–26]. Here, the magnetic field is produced by the photocurrents, and in contrast to applications in nanoscale nuclear magnetic resonance [24–26], we directly control both the frequency and the phase of the ac signal through the timing of the
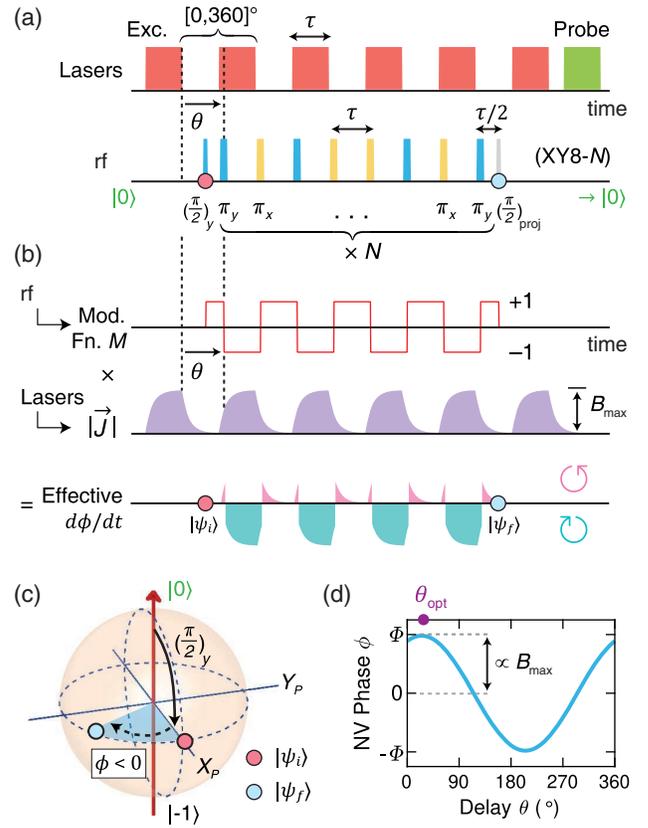

FIG. 2. Protocol for detecting ac photocurrents. (a) Synchronized photoexcitation and dynamical decoupling sequence. The MoS_2 excitation laser is gated at a rate $\nu_{\text{exc}} = 1/2\tau$, while an XY8-$N$ dynamical decoupling sequence with spacing τ between the π pulses is applied to the NV center spin. The delay between the first π pulse and the end of the last photoexcitation pulse is denoted as the phase θ (e.g., $\theta = 200°$ for the pulse trains shown). The rotation axes (x or y) of the rf pulses are color coded. The axis for the last $\pi/2$ projection pulse varies depending on which projection (X_P or Y_P) of the final superposition state is measured by the probe laser. (b) Schematic of the modulation function $M(t)$ and photocurrent density $|\vec{J}(t)|$ corresponding to the rf and photoexcitation pulses, respectively, shown in (a). The photocurrent density displays a rise and fall time and produces a time-varying magnetic field with amplitude B_{max} along the NV axis. The phase ϕ acquired by the NV center is the integral of the product of $M(t)$ with the photocurrent magnetic field (product shown in bottom trace). (c) Bloch-sphere representation of NV spin precession. The $(\pi/2)_y$ pulse prepares the initial state $|\psi_i\rangle$, which evolves to $|\psi_f\rangle$ during the sensing duration. (d) Simulated dependence of ϕ on the delay θ for a sinusoidal magnetic field. The maximum phase Φ is acquired at the optimal delay θ_{opt} and is determined by the magnitude B_{max} of the local magnetic field produced by the photocurrents.

photoexcitation pulses [Figs. 2(a) and 2(b)]. This control enables us to sweep the phase of the oscillating field relative to the NV sensing sequence, which increases the detection sensitivity compared to averaging the NV

response over random signal phases. From the initialized state $|0\rangle$, we prepare the NV center in the superposition $|\psi_i\rangle = 1/\sqrt{2}(|0\rangle + |-1\rangle)$ using a $\pi/2$ rotation [Fig. 2(c)]. Thereafter, the NV center precesses under the influence of the magnetic field produced by the pulsed photocurrents [Fig. 2(b), purple] and the π-pulse spin rotations of the XY8-N sequence (N repetitions of a block of eight π pulses). A final $\pi/2$ projection pulse [Fig. 2(a), gray] allows the accumulated phase ϕ of the final state $|\psi_f\rangle = 1/\sqrt{2}(|0\rangle + e^{i\phi}|-1\rangle)$ to be measured by the probe beam. The rotation axis of this final $\pi/2$ pulse converts either the X or Y projection of $|\psi_f\rangle$ [$X_P = \cos(\phi)$ and $Y_P = \sin(\phi)$] into a population difference between $|0\rangle$ and $|-1\rangle$, which is resolved by the PL intensity.

We first match the spacing τ between the π pulses to a half period of the photoexcitation rate $\nu_{\rm exc}$ ($=1/2\tau$ here) and probe the acquired phase ϕ for varying delays θ between the start of the π pulses and the photoexcitation [Fig. 2(a)]. The effect of the π pulses is to introduce a modulation function $M(t)$, which switches sign each time a π pulse is applied [Fig. 2(b)] [12]. The cumulative phase acquired by the NV center is the integral of the time-varying magnetic field multiplied by $M(t)$:

$$\phi = \int_{t_i}^{t_f} 2\pi\gamma B_\parallel(t) M(t - t_0) dt,$$

where $B_\parallel$ is the component of the photocurrent magnetic field along the NV center axis, $t_0 = \tau\theta/180°$, and $[t_i, t_f]$ corresponds to the sensing duration bounded by the two $\pi/2$ pulses. The delay θ in this "quantum lock-in" protocol thus tunes the amplitude of the NV precession [Fig. 2(d)],

analogous to the relative phase between the signal and reference oscillator in a classical lock-in detection. By sweeping θ, we determine the quantity Φ, defined as the extremal value of $\phi(\theta)$, the phase acquired by the NV, for $\theta \in [0, 180]°$. The amplitude and sign of Φ is determined by the amplitude and direction of the local current density. If photoexcitation generates an instantaneous, square-pulse current density $\vec{J}$ in the MoS$_2$ monolayer, then Φ occurs at the optimal delay $\theta_{\rm opt} = 0°$, where the photocurrent signal aligns with the sensing sequence. Instead, if the photocurrent rises and falls with a characteristic timescale [Fig. 2(b)], maximal phase accumulation will occur for nonzero optimal delay ($\theta_{\rm opt} > 0°$). For a current density $\vec{J}$ with sinusoidal time dependence, the accumulated phase is likewise sinusoidal: $\phi = \Phi\cos(\theta - \theta_{\rm opt})$ [Fig. 2(d)]. This form represents a good approximation to our data due to the smoothing effect of the photocurrent rise and fall times (see Supplemental Material Sec. 4 [29]).

III. RESULTS

A. Detection and mapping of photo-Nernst currents

We first perform a photocurrent sensing protocol with $N = 2$ and $\tau = 7.6$ μs over an uncovered area of diamond (with probe and excitation beams slightly offset). Consistent with negligible absorption by the NV center or bulk diamond at 661 nm, we cannot detect the presence of photoexcitation, and we measure $\phi = 0$ for all θ (Supplemental Material Fig. S7 [29]). Remarkably, when we shift to an area where monolayer MoS$_2$ covers the diamond, we detect oscillations in X_P and Y_P as θ is varied
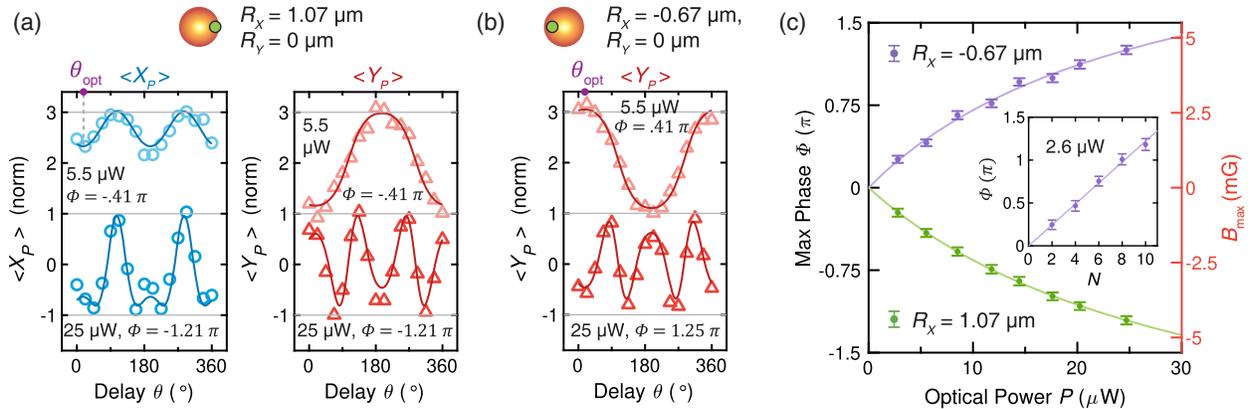

FIG. 3. NV spin precession due to ac magnetic field of local photocurrents. (a) Experimental X_P and Y_P projections of the final NV superposition state as the delay θ is varied for two different optical powers (synchronized sensing sequence with $N = 2$, $\tau = 7.6$ μs). The probe beam ($R_X = 1.07$ μm) is positioned to the right of the excitation beam over an area where MoS$_2$ covers the NV ensemble. The solid lines are simultaneous fits to both projections, allowing determination of Φ and $\theta_{\rm opt}$. (b) Same measurement but with the probe beam ($R_X = -0.67$ μm) to the left of the excitation beam. Note that X_P (not shown) looks similar to (a), but Y_P is inverted, indicating that the local photocurrent direction is reversed. (c) Dependence of the maximum phase Φ on the optical power P for $R_X = -0.67$ μm (purple) and $R_X = 1.07$ μm (green). The right-hand axis converts Φ to the maximal field amplitude, $B_{\rm max}$, along the NV axis due to the photocurrent pulses. Inset: Dependence of Φ on the number of repetitions N of the XY8-N sequence at $R_X = -0.67$ μm ($\tau = 7.6$ μs). All error bars presented in this paper are 95% confidence intervals.

[Fig. 3(a); $R_X = 1.07~\mu$m, $R_Y = 0~\mu$m], revealing the presence of an ac magnetic field due to photocurrents. Fitting the X_P and Y_P projections simultaneously to their expected behavior [solid lines in Fig. 3(a)], we deduce that the maximal phase Φ increases in magnitude as the photoexcitation power P increases and that the optimized delay θ_{opt} is nonzero [Fig. 3(a)], indicating a finite photocurrent rise time τ_{rise}. We rule out heating of the diamond substrate as the source of the acquired phase by showing that the phase accumulated by the initial state $|\psi_i\rangle = 1/\sqrt{2}(|0\rangle + |+1\rangle)$ is opposite to that by $1/\sqrt{2}(|0\rangle + |-1\rangle)$, while temperature-dependent shifts would affect both $|\pm 1\rangle$ identically (see Supplemental Material Fig. S8 [29]).

Strikingly, when the probe beam is moved to the opposite side of the excitation beam ($R_X = -0.67~\mu$m, $R_Y = 0~\mu$m), the phase accumulated by the NV center switches sign, signifying a reversal in the direction of the local photocurrent density $\vec{J}$ [Fig. 3(b)]. For both locations, we observe a sublinear dependence of the maximum phase Φ on the photoexcitation power [Fig. 3(c)]. This behavior is consistent with a PTE origin for the photocurrents as the thermal gradient induced in monolayer MoS$_2$ by laser heating begins to saturate in our thermal model (see Appendix D). The absence of any interface potentials that induce directional electric fields further suggests a PTE origin, which has been shown to be the dominant photocurrent generation mechanism in monolayer MoS$_2$ [16,17]. As expected, when the sensing duration is increased through the number of repetitions N of the XY8 block, Φ increases linearly [Fig. 3(c), inset].

By modeling $\vec{J}$ to have an exponential rise and fall time τ_{rise}, we estimate the maximum field B_{max} at the end of each excitation pulse [Fig. 2(b)] via

$$B_{\text{max}} = \beta \times \Phi/(0.5 \times 8N\tau \times 2\pi\gamma),$$

where β is a pulse-shape-dependent factor, Φ is measured in radians, and the factor of 0.5 stems from the 50% duty cycle of the photoexcitation (Appendix C). The factor β increases monotonically with τ_{rise} from $\beta = 1$ for square pulses to $\beta = 2$ as $\tau_{\text{rise}} \to \infty$. Unless otherwise stated, we use $\beta = 1.25$, corresponding roughly to the range of our typical measurements ($\tau_{\text{rise}} \sim 1~\mu$s, $\tau = 7.6~\mu$s). We resolve B_{max} as small as 0.84 ± 0.08 mG for about 2 hours of averaging time for data shown in Fig. 3(c), and 0.14 ± 0.05 mG for additional data in Appendix E. The latter measurement indicates that we can resolve uniform sheet currents of 20 nA/μm (flowing perpendicular to the NV axis on the surface plane), which produces a field $B_{\text{max}} \sim 0.1$ mG independent of the depth of the NV center. In comparison, Ref. [22] projects a detection limit of about 1 μA/μm for dc currents in graphene for a similar averaging time using widefield detection. In Appendix E, we estimate that this sample's sensitivity would be

200 nA/(μm $\sqrt{\text{Hz}}$) using an optimal protocol. The high sensitivity here is enabled by our synchronized dynamical decoupling protocol, which extends the NV ensemble's coherence time from $T_2^* = 0.51~\mu$s to $T_2(XY8-2) = 235~\mu$s and provides access to coherent oscillations in $Y_P = \sin(\phi)$, more sensitive than $X_P = \cos(\phi)$ to small ϕ.

In equilibrium, the divergence-free condition $\nabla \cdot \vec{J} = 0$ and rotational symmetry of our experiment imply that any photocurrent should flow as vortices around the excitation spot, explaining the reversal in the direction of $\vec{J}$ observed between Figs. 3(a) and 3(b). Nonzero photocurrent, defining a chirality to the vortex, requires the Lorentz force from the external magnetic field. We deem the resulting current profile a "photo-Nernst vortex" since the radial temperature gradient induced by the excitation beam and the out-of-plane B_{ext} results in azimuthal current flow, transverse to the temperature gradient, as expected for the Nernst effect. Previously, photo-Nernst currents [18,19] were detected by scanning photocurrent microscopy at the edges of exfoliated graphene devices. However, spatial mapping of an unperturbed vortex in the interior of a 2D material has not been possible as, notably, it generates zero net current in a transport measurement.

By scanning the probe beam relative to the excitation spot, we map the magnetic-field distribution inside the photo-Nernst vortex. In Figs. 4(a) and 4(b), we present the measured B_{max}, the component of the field parallel to the NV axis, for line scans along the x and y directions, respectively. Crucially, we show that B_{max} changes sign as expected when the static magnetic field B_{ext} is reversed, indicating that the chirality of the vortex also reverses [Fig. 4(a)]. The solid lines in Figs. 4(a) and 4(b) present the simulated field projection along the [111] axis at the NV center depth for a model of the photocurrent distribution $\vec{J}(R)$ (see Supplemental Material Sec. VII [29]). We assume an azimuthal flow with amplitude

$$|\vec{J}(R)| \propto \frac{d}{dR} e^{-(R^2/2\sigma_J^2)}$$

since $\vec{J}(R)$ is expected to be proportional to the gradient of an approximately Gaussian photo-induced temperature distribution. Although we phenomenologically incorporate deviations from a perfectly circular excitation beam to better match the experimental profile, the salient features of a vortex current density are clear. Here, B_{max} is nonzero at the vortex center due to the z component of the field produced by the current loops. Along the x direction, the measured B_{max} are asymmetric about the center since the rotationally symmetric fringing fields are projected onto an oblique, [111]-oriented NV axis situated below the MoS$_2$ monolayer [Fig. 4(a)]. For the y direction, the fringing fields are primarily perpendicular to the NV axis, and B_{max} is dominated by the z component of the field, which changes sign outside the ring of maximum current density [Fig. 4(b)].
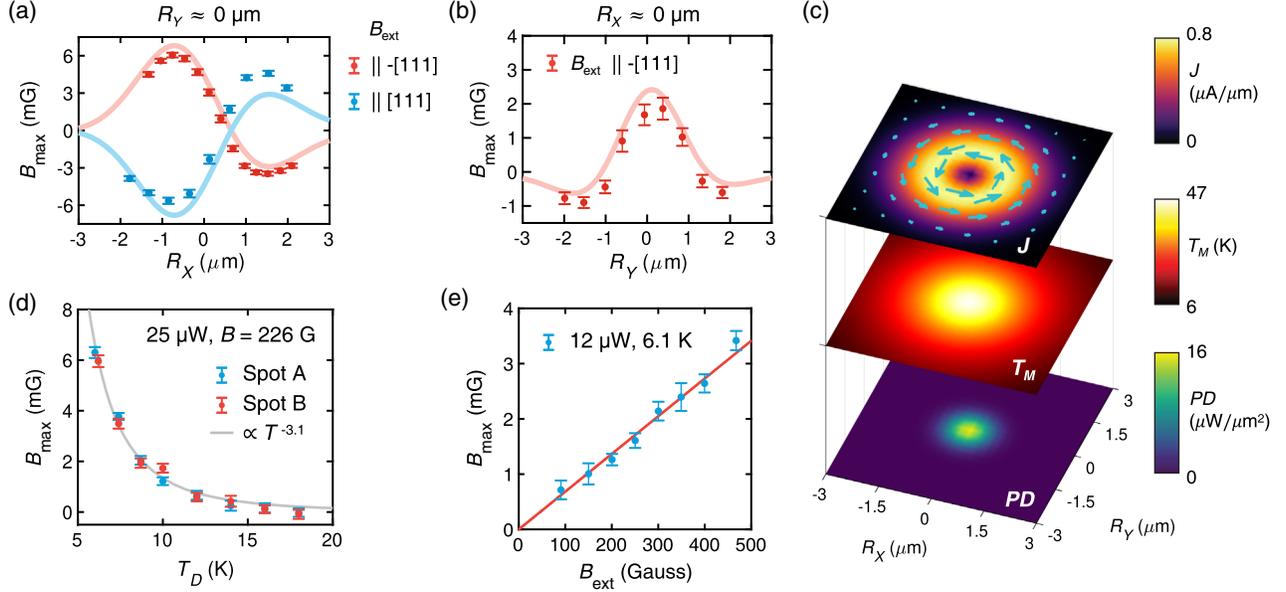
FIG. 4. Spatial mapping of a photo-Nernst vortex. (a) Line scan of B_{max}, the magnetic field parallel to the NV axis, along the x axis of the vortex ($R_Y \approx 0$ μm, $P = 25$ μW). Note that B_{max} is extracted from phase measurements while sweeping the delay θ. When the direction of the external magnetic field B_{ext} is reversed, B_{max} changes sign in accordance with the Nernst effect (here, we fix the positive field direction to be along [111]). (b) Line scan of B_{max} along the y axis ($R_X \approx 0$ μm). The solid lines in (a) and (b) are simulated stray fields along the NV axis for a modeled vortex current density $\vec{J}(R)$; slightly different parameters are used for (a) and (b). (c) Comparison of the current density model $\vec{J}(R)$ which best fits the data, the simulated laser-induced temperature distribution $T_M(R)$ in the monolayer MoS$_2$, and the power density PD(R) of the excitation beam for $P = 25$ μW, assuming rotational symmetry and using the measured excitation beam width. The spatial profile of $\vec{J}(R)$ is in close agreement with the temperature gradient $|dT_M(R)/dR|$. (d) Dependence of photo-Nernst currents on the diamond temperature T_D. Two different spots on the sample are measured with $R_X = -0.95$ μm. The decay in B_{max} is due to the change in the thermal properties of MoS$_2$ and its interface with diamond. The solid line is a power-law fit. (e) Dependence of B_{max} at $R_X = -0.95$ μm on the external field B_{ext}, parallel to the NV axis, for a second monolayer MoS$_2$ sample. Note that B_{max} scales linearly with B_{ext} as expected for the Nernst effect in low magnetic fields.

In Fig. 4(c), we plot the current distribution $\vec{J}(R)$ used to approximate the experimental field profile together with independent thermal modeling of the laser-induced temperature distribution $T_M(R)$ in monolayer MoS$_2$. The modeled $\vec{J}(R)$ peaks at $\sigma_J \sim 1.0$ μm, in close agreement with the predicted location of the maximum thermal gradient (Supplemental Material Fig. S11 [29]). At the diamond substrate's base temperature ($T_D = 6$ K), the photocurrent vortex is enhanced by the reduced thermal conductivity of monolayer MoS$_2$ and the diminished thermal interface conductance to the substrate, which permit large thermal gradients (~18 K/μm max) and a spatial distribution significantly larger than the excitation spot size (Gaussian standard deviation $\sigma_{exc} = 0.45$ μm). As T_D increases, the combined increase in thermal conductivity [34] and thermal interface conductance [35] is expected to reduce both the size and strength of the photocurrent vortex. Consequently, the detected B_{max} at $R_X = -0.95$ μm diminishes, disappearing around 20 K [Fig. 4(d)].

Integrating $\vec{J}(R)$ for positive R, we estimate that the current flowing in the vortex is about 1.3 μA for an excitation power of 25 μW before the objective (85% transmission). This result implies a Nernst photoresponsivity of about

60 mA/W for 226 G parallel to the NV axis (130 G perpendicular to the sample). This value for our ungated monolayer MoS$_2$ sample is about 3 times higher than the Nernst photoresponsivity reported at the same magnetic field for a graphene-hexagonal boron nitride heterostructure that is gate tuned to an electron-side van Hove singularity [19]. This enhancement in MoS$_2$ is consistent with its lower thermal conductivity and higher Seebeck coefficient stemming from a favorable density of states for its gapped band structure [16,17]. In Fig. 4(e), we verify that the Nernst photocurrent is linear in the external magnetic field B_{ext} and nonsaturating up to 500 G, as expected for the low-field regime [19].

B. Temporal dynamics of photo-Nernst currents

Our technique provides additional insight into the dynamics of photothermal carrier generation. In Fig. 5(a), we examine the optimal delay θ_{opt} as a function of R_X, using a sequence with $\tau = 7.6$ μs. As the probe beam moves away from the excitation spot, θ_{opt} increases. This effect can be explained if the rise time for the local photocurrent, which dominates the contribution to the local field, increases for larger $|R_X|$. To corroborate this hypothesis, we map the leading edge of the photocurrent rise by varying the pulse
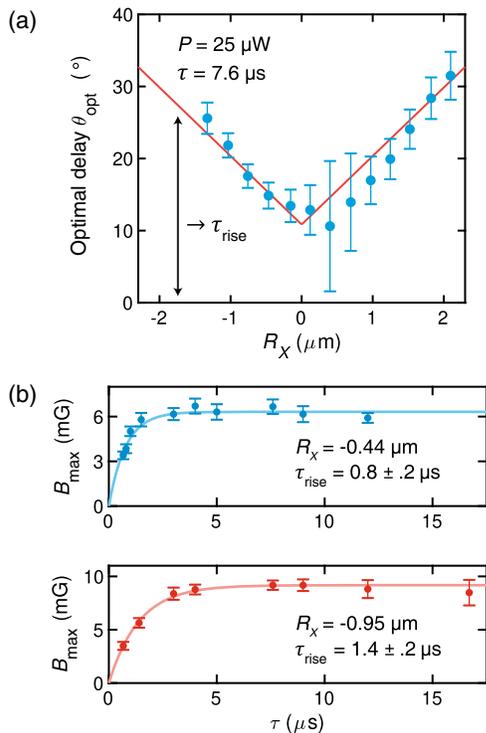
(a)

(b)

FIG. 5. Temporal dynamics of photo-Nernst current generation. (a) Dependence of the optimal delay θ_{opt} on the coordinate R_X for $R_Y = 0$. The linear fit (solid line) indicates that for increasing $|R_X|$, the photocurrent rise time τ_{rise} becomes a larger fraction of τ, the duration of a single photoexcitation pulse. (b) Measured B_{max} versus the spacing τ of the synchronized photosensing sequence for two different values of R_X using $P = 38 \ \mu W$. Here, the repetition rate of the photoexcitation and NV driving pulses remain equal, but they change together. The rise time τ_{rise} for B_{max} increases for larger $|R_X|$, corroborating the trend in θ_{opt} shown in (d). The solid lines are exponential fits.

spacing τ in the synchronized sensing protocol. To deduce B_{max}, we need to account for variations in pulse shape as τ changes. For each set with different τ, we utilize the measured delay θ_{opt} to infer the factor β within our pulse shape model. In Fig. 5(b), we compare $B_{max}(R, \tau)$ for two different locations. We confirm an exponential rise to the photocurrent with a time constant $\tau_{rise} \sim 1 \ \mu s$ that increases for larger $|R_X|$. The extracted rise times are sufficient to explain the measured θ_{opt} and are independent of the external magnetic field, suggesting that no additional effects, such as carrier propagation from the excitation spot, contribute significantly to the delay (Supplemental Material Sec. V [29]). The temporal resolution achieved by varying the pulse spacing τ is limited to about 100 ns by the finite duration of the NV π pulses [36]; however, our "quantum lock-in" sequence is compatible with ultrafast pump-probe optical excitation to investigate photocurrent dynamics at subpicosecond timescales (Supplemental Material Sec. VIII [29]).

The rise times for B_{max} can be compared to a model of the system's transient thermal response. Our simulations

confirm that the rise time for the thermal gradient $dT_M(R)/dR$ increases for larger $|R|$ (see Appendix D), thus supporting the picture of photocurrents generated locally by the PTE. Interestingly, to approximate the microsecond-scale photocurrent rise times, we need to assume a heat capacity c_p for monolayer MoS_2 that is significantly higher than theoretically predicted [37,38]. Our model estimates $c_p \sim 200 \ J/(kg \ K^2) \times T_M$ for temperatures below about 50 K, while c_p is generally taken [16] as 400 $J/(kg \ K)$ for single-crystal monolayer MoS_2 at 300 K. Even considering that we use polycrystalline MoS_2, this discrepancy may suggest extrinsic contributions to the estimated c_p. For example, excess heat capacity could arise from PMMA residue or a layer of cryopumped adsorbates, and the latter is known to significantly raise the measured low-temperature heat capacity of other low-dimensional materials [39,40] (Supplemental Material Fig. S2 [29]). Further investigations under systematic outgassing and sample cleaning conditions are required to clarify this phenomenon or to explore its use for the sensing of absorbed gases.

Finally, we demonstrate the ability to detect light without prior knowledge of its repetition rate or phase. Gating the light at a constant rate ν_{exc} with an independent controller, we examine the projection X_P of the final state $|\psi_f\rangle$ as we scan the spacing τ of an XY8-8 sequence. When the frequency $\nu = 1/2\tau$ of the decoupling sequence matches ν_{exc} to within a bandwidth $\Delta\nu \approx 0.11/N\tau$, the average value of X_P over random starting delays θ is diminished from its initial full projection, resulting in a resonant dip [25]. In Fig. 6, we demonstrate this unsynchronized detection
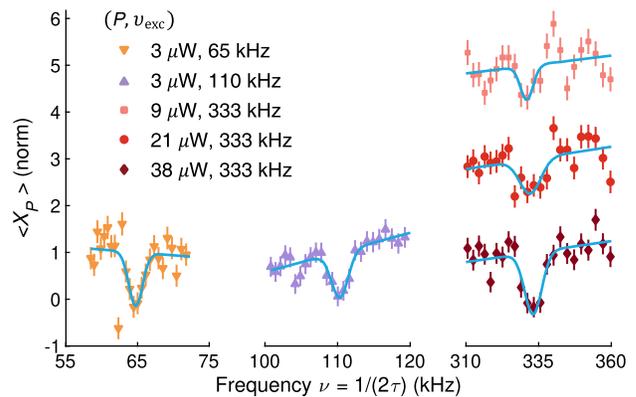

FIG. 6. Detection of unsynchronized, variable-frequency ac photocurrents. We show the X projection of the final NV state using an unsynchronized XY8-8 sensing sequence. The photoexcitation repetition rate ν_{exc} is fixed for each set, and the repetition rate of the NV driving pulses $\nu = 1/2\tau$ is scanned. When ν approaches resonance with ν_{exc}, the projection X_P displays a dip when averaged over repetitions with a random relative phase between the photoexcitation and NV driving pulses. Data for three different photoexcitation frequencies $\nu_{exc} = 65$ kHz, 110 kHz, and 333 kHz are shown. The amplitude of the resonant dip is sensitive to the photoexcitation power P.

scheme for three different frequencies: $\nu_{\text{exc}} = 65$ kHz, 110 kHz, and 333 kHz. Because of the rise time of the PTE photocurrents, our sensitivity to optical power decreases for higher ν_{exc}, necessitating stronger excitation to see the same contrast change. However, the NV sensing protocol itself is effective for frequencies up to several tens of MHz [36] and thus can be combined with faster photocurrent mechanisms for optimal photodetection.

IV. DISCUSSION

Our demonstration broaches wide-ranging opportunities for investigating fascinating opto-electronic phenomena in materials. Highlighted by our mapping of a photo-Nernst vortex, the ability to spatially resolve photocurrent flow could more clearly characterize phenomena obscured in transport-based techniques, including chiral photocurrents localized at edges [41], directional currents controlled by coherent optical injection [42], and the scattering of valley-polarized [4], Weyl-point [8–10], or Dirac-point [11] photocurrents from disorder. Beyond fundamental interests, nano-engineering of the diamond surface into pillared arrays [43,44] would reduce the thermal interface conductance and possibly extend the results here to room temperature. As an additional benefit, the waveguiding effect of these pillars would significantly enhance photon collection efficiency to reduce averaging times. This result, in conjunction with the use of wide-field imaging techniques [22] and isotopically purified samples [45] that prolong the NV's quantum coherence, could enable ultrasensitive, large-area photodetector arrays using our technique. Moreover, the optical generation of ac magnetic fields that are spatially localized, but also available on demand anywhere across the area covered by MoS$_2$, provides simplified, stick-on alternatives for fabricating devices to manipulate solid-state spins. Adding to capabilities such as electrical spin readout [46], spontaneous emission tuning [47], and 2D ferromagnetism [48], our demonstration of spin-photocurrent interaction widens the perspective for integrated quantum technologies based on the quantum emitter-2D material platform.

APPENDIX A: SAMPLE FABRICATION

A NV center ensemble was created about 40 nm deep into an [001]-oriented diamond sample by $^{15}\text{N}^+$ ion implantation. The implantation energy was 30 keV, with an area dose of 10^{12} ions/cm^2. The samples were annealed at 850 °C and then 1100 °C to form roughly 85 NVs per optical spot. The external field B_{ext} was supplied by a permanent magnet, and microwave pulses were delivered by a wire coil suspended above the sample surface.

Monolayer MoS$_2$ was grown on SiO$_2$/Si via MOCVD. It was then spin coated with PMMA and baked at 180 °C. After applying thermal release tape (TRT), the stack was mechanically peeled off the SiO$_2$/Si substrate and transferred to the diamond in a vacuum chamber. Lastly, the TRT and PMMA were removed. Three separate MoS$_2$ samples were transferred and investigated in this work, all displaying NV-based photocurrent detection.

Further details of the sample growth and fabrication can be found in the Supplemental Material [29].

APPENDIX B: NV PHOTOCURRENT SENSING TECHNIQUE

The photocurrent sensing sequence consists of simultaneous ac optical excitation of the monolayer MoS$_2$ and dynamical decoupling pulses applied to the NV center spin. A 532-nm laser initializes the NV center spin into $m_s = |0\rangle$ via relaxation through a state-selective, spin-flip decay channel and enables optical spin readout by spin-dependent PL. In addition, a 661-nm laser is used to excite photocurrents in monolayer MoS$_2$ by PTE. Both lasers were focused by an objective onto the sample held at 6 K inside a closed-cycle cryostat (Montana Instruments). The 661-nm laser spot was laterally displaced by impinging on the objective's back aperture at a slight angle away from normal. The displacement was measured by collecting reflected light off the sample into a camera and determining the center locations of the beams using calibrated pixel sizes. The 661-nm excitation was pulsed by modulating its polarization with an electro-optical modulator and passing the output through a Glan-Thompson polarizer. The polarization of the 661-nm beam was thereafter set to be right circularly polarized; however, the results here are not dependent on the polarization.

After optically initializing the NV spin into $|0\rangle$, the XY8-N dynamical decoupling sequence applied to the NV center consists of $8N + 2$ qubit rotations:

$$\left(\frac{\pi}{2}\right)_y - [\pi_y - \pi_x - \pi_y - \pi_x - \pi_x - \pi_y - \pi_x - \pi_y]^N - \left(\frac{\pi}{2}\right)_{\text{proj}}.$$

Here, the subscript indicates the axis on the Bloch sphere for the qubit rotation, and $\{\pi/2, \pi\}$ indicates the rotation

angle. The alternation of the rotation axes for the π pulses is designed to mitigate pulse errors. The rotation axis of the final $\pi/2$ projection pulse is varied between $\pm X$ and $\pm Y$ in order to measure the Y_P and X_P projections, respectively, of the final superposition state $|\psi_f\rangle$ in differential mode. The projection pulse rotates the selected equatorial component of $|\psi_f\rangle$ onto the Z axis of the Bloch sphere, corresponding to a population difference between the $|0\rangle$ and $|-1\rangle$ qubit states. This spin polarization is then distinguished by the NV center's spin-dependent PL intensity. The π pulses are uniformly spaced by the interval τ, whereas the $\pi/2$ pulses are spaced from the π pulses by $\tau/2$. The timing (repetition rate, delay) of the photoexcitation and NV microwave pulses is synchronously controlled with nanosecond resolution using an arbitrary waveform generator. The 532-nm spin-readout laser also generates photothermal currents in MoS_2; however, these currents do not affect our measurement results because they occur outside of the sensing duration.

APPENDIX C: PHOTOCURRENT RISE TIME MODEL

The XY8-N sequence introduces the following modulation function,

$$M(t/\tau) = \begin{cases} -1, & \text{for } 0 \leq \text{mod}\,(t/\tau - 0.5, 2) < 1 \\ +1 & \text{for } 1 \leq \text{mod}\,(t/\tau - 0.5, 2) < 2 \end{cases}$$

which leads to phase accumulation ϕ on the initial NV center spin superposition according to

$$\phi = \int_{t_0}^{t_0+8N\tau} \gamma B_\|(t) M(t - t_0) dt,$$

where τ is the XY8-N pulse interval, $t_0 = \tau\theta/\pi$, and here $\gamma = 2\pi \times 2.8$ MHz/Gauss. First, we consider a sinusoidal

photocurrent signal with period 2τ, which produces a field $B_\| = B_{\max}(\cos(\pi t/\tau) + 1)/2$, with amplitude $B_{\max}$. In this scenario, the phase accumulation is likewise a sinusoidal function of the relative phase (θ) between signal and sensor:

$$\phi_{\sin}(B_{\max}, \theta) = \gamma T(2/\pi) B_{\max} \cos\theta,$$

where we define $T = 0.5 \times 8N\tau$ to be the sensing duration multiplied by a 50% duty cycle (which will be useful later). At the end of the sensing sequence, the x and y components of ϕ are measured, leading to a simultaneous fit of two data sets with parameters $\{\Phi, \theta_{\text{opt}}, A, C\}$:

$$X_p(\theta) = A \cos\left(\Phi \cos(\theta - \theta_{\text{opt}})\right) + C,$$

$$Y_p(\theta) = A \sin\left(\Phi \cos(\theta - \theta_{\text{opt}})\right) + C.$$

Here, A and C are the normalized contrast and offset, expected to be 1 and 0, respectively. For the case of a sinusoidal signal, θ_{opt} is expected to be 0, and the maximum phase accumulation Φ is $\gamma T(2/\pi)B_{\max}$. We define the scaling factor $\beta \equiv \gamma T B_{\max}/\Phi$ as the ratio between the amplitude of the signal field ($B_{\max}$) to the amplitude of the phase response normalized by γT. Hence, for a sinusoidal signal field, $\beta = \pi/2$. In Supplemental Material Sec. IV. 2 [29], $X_p(\Phi, \theta)$ and $Y_p(\Phi, \theta)$ for a sinusoidal signal are plotted.

For fields generated by our pulsed photocurrents (50% duty cycle), the resulting field profile is expected to demonstrate an exponential rise and fall time (Fig. 9). In this case, we parametrize the shape of $B_\|$ (within one period) by

$$B_\|(t) = \begin{cases} B_{\max}(1 - A_0)^{-1}\left(1 - \exp(-t/\tau_{\text{rise}})\right), & \text{for } 0 \leq t < \tau \\ B_{\max}(1 - A_0)^{-1}\left(\exp(-(t - \tau)/\tau_{\text{rise}}) - A_0\right), & \text{for } \tau \leq t < 2\tau, \end{cases}$$

where the constant $A_0 \equiv \exp(-\tau/\tau_{\text{rise}})$, such that the maximum amplitude of this signal is also $B_{\max}$. In Fig. S4 of the Supplemental Material, we plot this pulse shape along with the calculated $\phi(\theta)$ acquired by the NV center for exemplary values of τ_{rise}/τ. We observe that for our typical range of rise times, the response $\phi(\theta)$ is well approximated by a phase-shifted sinusoid $\Phi \cos(\theta - \theta_{\text{opt}})$. For increasing rise time, θ_{opt} increases from zero as the photocurrent lags behind the excitation pulse. In the limit of long rise time, where the signal becomes triangular, θ_{opt} approaches a 90° shift

[Fig. 7(a)]. In addition, the scaling factor β between the maximum of the signal, $B_{\max}$, and the maximum of the phase response, Φ, also increases with increasing τ_{rise}/τ, which reflects the fact that Φ is reduced as the signal is spread over the response function. In Fig. 7(b), we plot β, showing it to be equal to 1 for zero rise time (square pulses) and to approach 2 in the limit of long rise time. Combining the information in Figs. 7(a) and 7(b), we can use θ_{opt} to determine $\beta(\theta_{\text{opt}})$ [Fig. 7(c)]. Thus, within this pulse shape model, the fit values of Φ and θ_{opt} can be used to compute $B_{\max}$.
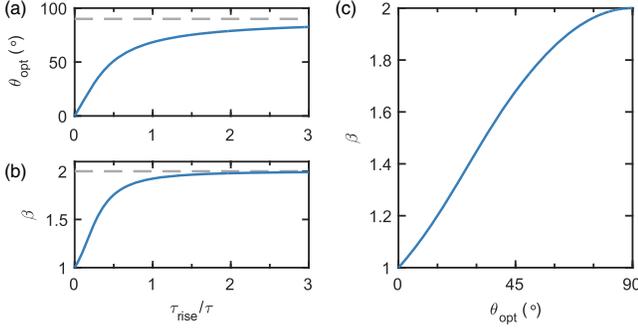
FIG. 7.   Dependence of the NV phase response on the photocurrent rise time. (a) Analytic value of optimal delay θ_{opt} for an exponential rise and fall signal, as a function of the normalized rise time, τ_{rise}/τ. The limit $\tau_{\text{rise}} \to 0$ is a square wave signal, whereas $\tau_{\text{rise}} \to \infty$ represents a triangle wave signal, where θ_{opt} approaches 90°. (b) Analytic value of $\beta \propto B_{\text{max}}/\Phi$ as a function of rise time. In the limit of a triangle wave signal, β approaches 2. (c) β determined from θ_{opt} using (a) and (b). The factor β allows the amplitude of the field B_{max}, reached at the end of the pulse, to be determined from the time-integrated phase Φ accumulated by the NV center.

APPENDIX D: THERMAL MODELING

We adopt a two-dimensional model for the laser-induced heating of monolayer MoS_2 on top of a diamond substrate [16,49]. We assume the system to be rotationally symmetric around the laser spot and incorporate an interfacial heat transfer to the diamond substrate fixed at constant temperature. The assumption that diamond acts as a constant temperature thermal bath is approximately valid due to diamond's high thermal conductivity, its low absorption of the 661-nm excitation wavelength, and thus the low total optical power absorbed by the system ($\sim\mu$W) in comparison to the cooling power of the cold finger.

Under these assumptions, the 2D heat equation describing our system is

$$\rho c_p \frac{\partial T_M(R,t)}{\partial t} - \kappa \frac{1}{R}\frac{d}{dR}\left[R\frac{dT_M(R,t)}{dR}\right]$$
$$+ \frac{G}{d}[T_M(R,t) - T_D] = f(R).$$

where $T_M(R,t)$ is the time-dependent temperature of the monolayer MoS_2, R is the radial coordinate, ρ is the density of monolayer MoS_2, $c_p(T_M)$ is its temperature-dependent specific heat capacity, $\kappa(T_M)$ is its temperature-dependent thermal conductivity, d is the thickness of the monolayer, G is the thermal interface conductance between monolayer MoS_2 and diamond, T_D is the temperature of the diamond substrate, and $f(R)$ is the volumetric laser heating source. With the exception of c_p, all parameter values are taken from literature sources or determined by our measurements (see Supplemental Material Sec. VI [29]). We estimate c_p by requiring the model to approximately reproduce the rise times in the photocurrent data [Fig. 5(b)]. Here, we caution that the cryogenic heat capacity of low-dimensional materials is highly sensitive to cooldown conditions [39,40]. We simulate our model using the MATLAB PDE toolbox with Dirichlet boundary conditions $(T_M(R) - T_D = 0)$ on a square grid with edges at ±10 μm and a grid resolution of 0.2 μm.

In Fig. 8, we display the simulated temperature profile in monolayer MoS_2 as a function of the incident laser power P. Here, we choose $T_D = 9$ K to be slightly higher than the 6-K base diamond temperature to incorporate additional steady-state heating of $1L$-MoS_2. We present more detailed simulations incorporating transient effects in Fig. 9 for the specific optical power of 25 μW. The simulations indicate that the thermal gradient dT_M/dR saturates with increasing optical power [Fig. 8(c)]. This behavior matches the experimental data for the magnetic field B_{max} produced by the photocurrents and thus supports the conclusion that the photocurrents are driven by the PTE.
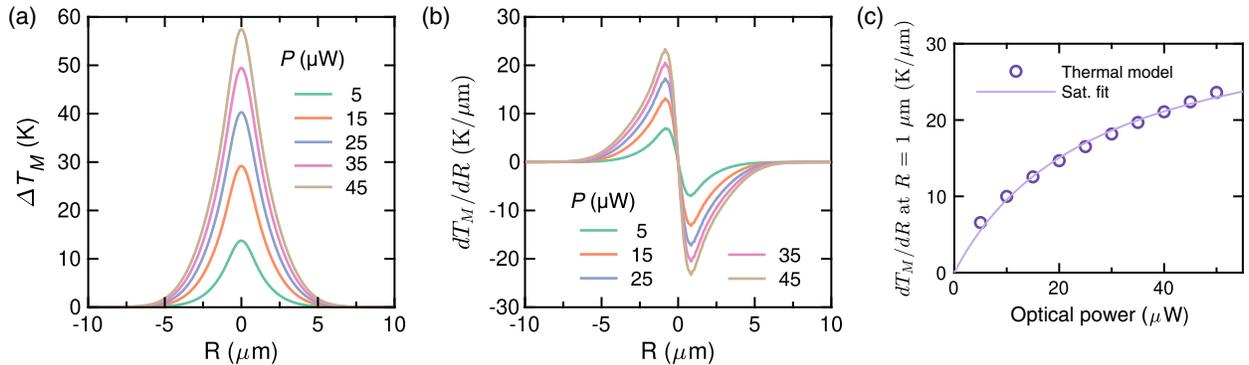

FIG. 8.   Simulated temperature profile in $1L$-MoS_2. (a) The temperature distribution $T_M(R)$ in $1L$-MoS_2 at the end of an excitation pulse of optical power P lasting $\tau = 7.6$ μs. The plotted y axis $\Delta T_M(R)$ is the rise in temperature from an initial uniform value of 9 K. (b) Spatial dependence of the thermal gradient dT_M/dR for various optical powers. (c) Dependence of the thermal gradient at $R = 1$ μm, near the maximum of dT_M/dR, versus optical power P. A sublinear, saturating behavior is observed in the simulations, in correspondence with the experimental data for the stray field measured by the NV [Fig. 3(c)].
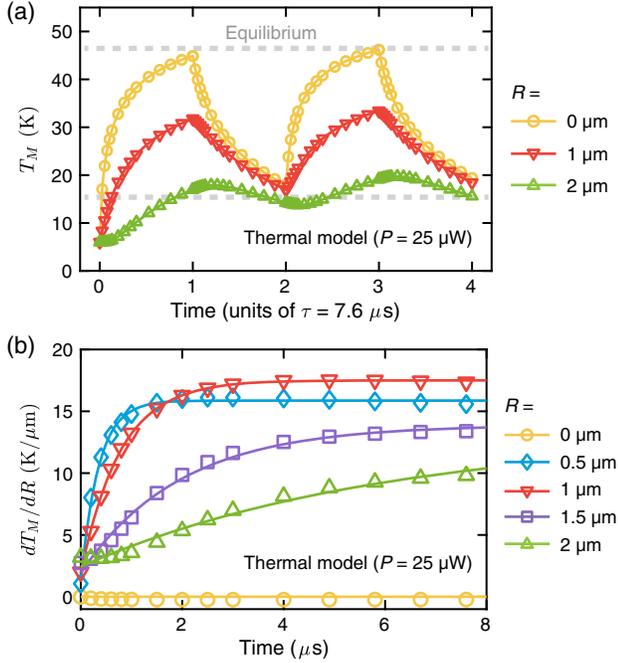
FIG. 9. Simulated thermal time dynamics. (a) Time-dependent heating and cooling of $1L$-MoS$_2$ during the first two excitation pulse cycles for $\tau = 7.6\ \mu$s and an excitation power of 25 μW. The ending condition for panel (a) is used as the starting point of panel (b) (i.e., after two pulse cycles). (b) Simulated dependence of the thermal gradient dT_M/dR versus the radial coordinate R for the third heating cycle, which approaches the equilibrium distribution. The solid lines are fits to $A\{1 - \exp[-(t/\tau_{\text{rise}})]\} + C$. The fitted rise times τ_{rise} for $dT_M/dR(R)$ are 0.35, 0.8, 2.0, and 6.0 μs for $R = 0.5$, 1, 1.5, and 2 μm, respectively. The increasing rise time for the thermal gradient for larger $|R|$ and its microsecond timescale are consistent with data for the stray magnetic field B_{max} due to the photocurrents (Fig. 5).

In Fig. 9, we present the simulated temporal response of the temperature profile in monolayer MoS$_2$. Starting with an initial temperature $T_M(R) = 6$ K, in equilibrium with the diamond substrate, we simulate the first two excitation pulses and their subsequent cooldown [Fig. 9(a)]. The MoS$_2$ sample does not cool back down to the substrate temperature but approaches the equilibrium temperature distribution after about two cycles. In Fig. 9(b), which approximates equilibrium, we show that the rise time in the thermal gradient $dT_M/dR(R)$ is longer for locations farther away from the center of the excitation beam. These rise times cannot be compared with the rise times in B_{max} exactly since the stray magnetic field is an integral of the photocurrent over all of space, with photocurrent intensity proportional to the absolute value of the thermal gradient. However, it is clear that the trend of increasing photocurrent rise times for larger $|R|$ is reproduced by the simulations and that the estimated heat capacity $c_p(T_M) = c_p \sim 200$ J/(kg K^2) $\times T_M$ produces τ_{rise} on the order of 1 μs, as observed in the experiment.

APPENDIX E: PHOTOCURRENT SENSITIVITY ESTIMATION

In Fig. 10, we show data that detect a minimum ac field of about 0.1 mG (peak-to-peak amplitude) along the NV axis in 2 hours of averaging time. The contrast in $Y_P = \sin(\phi)$ is what allows us to determine the small acquired phase, as $X_P = \cos(\phi)$ is nearly featureless. This case highlights the importance of not averaging over random signal delays θ since averaging Y_P over θ yields zero. To translate this minimum detected magnetic field to a current density, we assume that the magnetic field is generated by an infinite sheet current and hence is independent of the NV center depth. Practically, the field calculated using the infinite sheet model will be approximately correct as long as the sheet current density is uniform for an extent greater than the NV center depth (40 nm for the sample used here). We assume the sheet current to flow in the direction perpendicular to the NV axis (projected onto the 2D plane) so that the stray field from the currents is maximally aligned with the NV axis ([111]). In this case, the magnetic field of the sheet current flowing along $[1\bar{1}0]$ is then given by

$$\vec{B}_{\text{sheet}} = \frac{\mu_0 J_{\text{sheet}}}{2} \cdot [110]$$

$$B_{\text{max}} = \vec{B}_{\text{sheet}} \cdot \hat{n}_{NV} = \frac{2}{\sqrt{6}} \frac{\mu_0 J_{\text{sheet}}}{2}$$

For $B_{\text{max}} = 0.1$ mG, we obtain $J_{\text{sheet}} = 20$ nA/μm, setting the minimum sheet current density that we can detect in 2 hours by our current unoptimized measurement and fit procedure. As evident in Fig. 10 (blue curve), the X_P
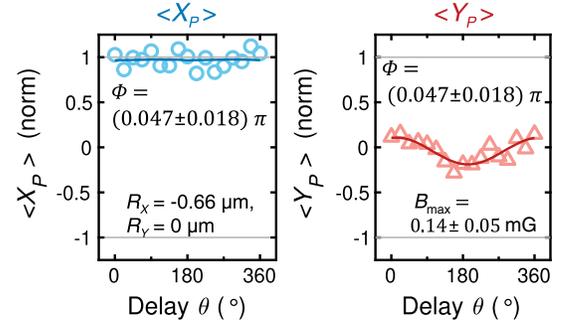

FIG. 10. Minimum photocurrent density measured. Data set showing a small phase acquired on device B for a total of 2 hours of averaging time. The sensing sequence here is XY8-2, with $\tau = 9\ \mu$s, $P = 6\ \mu$W, and $B_{\text{ext}} = 201$ G. The extracted maximal phase $\Phi = (0.047 \pm 0.018)\pi$ corresponds to a maximal projected field along the NV center axis of $B_{\text{max}} = 0.14 \pm 0.05$ mG using $\beta \approx 1.2$ (estimated from the θ_{opt} of the data set). This case corresponds to the field produced by a uniform sheet current density $J_{\text{sheet}} \approx 20$ nA/μm flowing perpendicularly to the NV axis.

projections are not sensitive to small phases and should be eliminated altogether, cutting measurement time in half without any loss.

The best magnetic-field sensitivity per $\sqrt{\text{Hz}}$ is obtained by taking the one data point where the rate of change of the signal versus magnetic field is steepest. This data point is the Y_P projection of $|\psi_f\rangle$ for $\theta = \theta_{\text{opt}}$. For this optimal measurement, the magnetic sensitivity [50] of the phase-locked XY8-N sequence is

$$B_{\min}(t) = \frac{\sigma(t)}{dS/dB_0},$$

where $\sigma(t)$ is the standard deviation in the signal S for time t of measurement, and dS/dB_0 is the maximized rate of change of the signal versus the field amplitude B_0. Considering an instantaneous, square-wave photocurrent with 50% duty cycle, amplitude B_0, and period 2τ, the maximum accumulated phase of the XY8-N sensing sequence occurs at $\theta_{\text{opt}} = 0°$ and is given by

$$\Phi = 2\pi\gamma \times T_\phi \times B_0/2,$$

where $T_\phi = 8N\tau$ is the total phase acquisition time. For small phases, the Y projection $Y_P = A\sin(\Phi(B_0))$ has the steepest slope versus dB_0; hence,

$$\frac{dY_P}{dB_0} = A\pi\gamma T_\phi$$

at $B_0 = 0$, and $A = CN_{\text{photons}}(t)$ is related to the PL contrast in raw counts. Here, $N_{\text{photons}}(t)$ is the total number of photons counted in the measurement time t and $2C$ is the percent contrast between the bright $|0\rangle$ and dark $|-1\rangle$ qubit states. For our photon count rates, the standard deviation $\sigma(t)$ is photon shot noise limited, and hence

$$\sigma(t) = \sqrt{N_{\text{photons}}(t)},$$

This result gives

$$B_{\min}(t) = \frac{1}{C\pi\gamma T_\phi \sqrt{k_{\text{photons}}t}}.$$

where k_{photons} is the number of readout photons we collect per second. Using our typical values ($C = 0.01$, $T_\phi \approx 150~\mu$s, and $k_{\text{photons}} = 0.75$ photons/rep $\times$ 6667 reps/s $\sim$ 5000 Hz), we obtain

$$B_{\min}(t)\sqrt{t} = 1.1~\frac{\text{mG}}{\sqrt{\text{Hz}}} = 110~\frac{\text{nT}}{\sqrt{\text{Hz}}}.$$

This magnetic-field sensitivity corresponds to a sensitivity of about 200 nA/(μm $\sqrt{\text{Hz}}$) for the density of uniform sheet currents flowing perpendicular to the NV center axis. We note that there is significant room for improvement in sensitivity by using higher-density ensembles with longer coherence times and engineering higher photon collection efficiency.

[1] F. H. L. Koppens, T. Mueller, P. Avouris, a C. Ferrari, M. S. Vitiello, and M. Polini, *Photodetectors Based on Graphene, Other Two-Dimensional Materials and Hybrid Systems*, Nat. Nanotechnol. **9**, 780 (2014).

[2] K. F. Mak and J. Shan, *Photonics and Optoelectronics of 2D Semiconductor Transition Metal Dichalcogenides*, Nat. Photonics **10**, 216 (2016).

[3] Y. Liu, N. O. Weiss, X. Duan, H.-C. Cheng, Y. Huang, and D. Xiangfeng, *Van der Waals Heterostructures and Devices*, Nat. Rev. Mater. **1**, 16042 (2016).

[4] K. F. Mak, K. L. McGill, J. Park, and P. L. McEuen, *The Valley Hall Effect in* MoS$_2$ *Transistors*, Science **344**, 1489 (2014).

[5] Z. Ye, D. Sun, and T. F. Heinz, *Optical Manipulation of Valley Pseudospin*, Nat. Phys. **13**, 26 (2017).

[6] H. Yuan, X. Wang, B. Lian, H. Zhang, X. Fang, B. Shen, G. Xu, Y. Xu, S.-C. Zhang, H. Y. Hwang, and Y. Cui, *Generation and Electric Control of Spin–Valley-Coupled Circular Photogalvanic Current in* WSe$_2$, Nat. Nanotechnol. **9**, 851 (2014).

[7] M. Eginligil, B. Cao, Z. Wang, X. Shen, C. Cong, J. Shang, C. Soci, and T. Yu, *Dichroic Spin–Valley Photocurrent in Monolayer Molybdenum Disulphide*, Nat. Commun. **6**, 7636 (2015).

[8] Q. Ma, S.-Y. Xu, C.-K. Chan, C.-L. Zhang, G. Chang, Y. Lin, W. Xie, T. Palacios, H. Lin, S. Jia, P. A. Lee, P. Jarillo-Herrero, and N. Gedik, *Direct Optical Detection of Weyl Fermion Chirality in a Topological Semimetal*, Nat. Phys. **13**, 842 (2017).

[9] G. B. Osterhoudt, L. K. Diebel, M. J. Gray, X. Yang, J. Stanco, X. Huang, B. Shen, N. Ni, P. J. W. Moll, Y. Ran, and K. S. Burch, *Colossal Mid-Infrared Bulk Photovoltaic Effect in a Type-I Weyl Semimetal*, Nat. Mater. **18**, 471 (2019).

[10] J. Ma, Q. Gu, Y. Liu, J. Lai, P. Yu, X. Zhuo, Z. Liu, J.-H. Chen, J. Feng, and D. Sun, *Nonlinear Photoresponse of Type-II Weyl Semimetals*, Nat. Mater. **18**, 476 (2019).

[11] Q. Ma, C. H. Lui, J. C. W. Song, Y. Lin, J. F. Kong, Y. Cao, T. H. Dinh, N. L. Nair, W. Fang, K. Watanabe, T. Taniguchi, S.-Y. Xu, J. Kong, T. Palacios, N. Gedik, N. M. Gabor, and P. Jarillo-Herrero, *Giant Intrinsic Photoresponse in Pristine Graphene*, Nat. Nanotechnol. **14**, 145 (2019).

[12] C. L. Degen, F. Reinhard, and P. Cappellaro, *Quantum Sensing*, Rev. Mod. Phys. **89**, 035002 (2017).

[13] F. Casola, T. van der Sar, and A. Yacoby, *Probing Condensed Matter Physics with Magnetometry Based on Nitrogen-Vacancy Centres in Diamond*, Nat. Rev. Mater. **3**, 17088 (2018).

[14] D. D. Awschalom, R. Hanson, J. Wrachtrup, and B. B. Zhou, *Quantum Technologies with Optically Interfaced Solid-State Spins*, Nat. Photonics **12**, 516 (2018).

[15] K. Kang, S. Xie, L. Huang, Y. Han, P. Y. Huang, K. F. Mak, C.-J. Kim, D. Muller, and J. Park, *High-Mobility Three-Atom-Thick Semiconducting Films with Wafer-Scale Homogeneity*, Nature (London) **520**, 656 (2015).

[16] M. Buscema, M. Barkelid, V. Zwiller, H. S. J. van der Zant, G. A. Steele, and A. Castellanos-Gomez, *Large and Tunable Photothermoelectric Effect in Single-Layer* MoS_2, Nano Lett. **13**, 358 (2013).

[17] K. Hippalgaonkar, Y. Wang, Y. Ye, D. Y. Qiu, H. Zhu, Y. Wang, J. Moore, S. G. Louie, and X. Zhang, *High Thermoelectric Power Factor in Two-Dimensional Crystals of* MoS_2, Phys. Rev. B **95**, 115407 (2017).

[18] H. Cao, G. Aivazian, Z. Fei, J. Ross, D. H. Cobden, and X. Xu, *Photo-Nernst Current in Graphene*, Nat. Phys. **12**, 236 (2016).

[19] S. Wu, L. Wang, Y. Lai, W. Shan, G. Aivazian, X. Zhang, T. Taniguchi, K. Watanabe, D. Xiao, C. Dean, J. Hone, Z. Li, and X. Xu, *Multiple Hot-Carrier Collection in Photo-Excited Graphene Moiré Superlattices*, Sci. Adv. **2**, e1600002 (2016).

[20] L. Thiel, D. Rohner, M. Ganzhorn, P. Appel, E. Neu, B. Müller, R. Kleiner, D. Koelle, and P. Maletinsky, *Quantitative Nanoscale Vortex Imaging Using a Cryogenic Quantum Magnetometer*, Nat. Nanotechnol. **11**, 677 (2016).

[21] M. Pelliccione, A. Jenkins, P. Ovartchaiyapong, C. Reetz, E. Emmanouilidou, N. Ni, and A. C. B. Jayich, *Scanned Probe Imaging of Nanoscale Magnetism at Cryogenic Temperatures with a Single-Spin Quantum Sensor*, Nat. Nanotechnol. **11**, 700 (2016).

[22] J. Tetienne, N. Dontschuk, D. A. Broadway, A. Stacey, D. A. Simpson, and L. C. L. Hollenberg, *Quantum Imaging of Current Flow in Graphene*, Sci. Adv. **3**, e1602429 (2017).

[23] K. Chang, A. Eichler, J. Rhensius, L. Lorenzelli, and C. L. Degen, *Nanoscale Imaging of Current Density with a Single-Spin Magnetometer*, Nano Lett. **17**, 2367 (2017).

[24] T. Staudacher, F. Shi, S. Pezzagna, J. Meijer, J. Du, C. a Meriles, F. Reinhard, and J. Wrachtrup, *Nuclear Magnetic Resonance Spectroscopy on a* $(5 - \text{nanometer})^3$ *Sample Volume*, Science **339**, 561 (2013).

[25] S. J. DeVience, L. M. Pham, I. Lovchinsky, A. O. Sushkov, N. Bar-Gill, C. Belthangady, F. Casola, M. Corbett, H. Zhang, M. Lukin, H. Park, A. Yacoby, and R. L. Walsworth, *Nanoscale NMR Spectroscopy and Imaging of Multiple Nuclear Species*, Nat. Nanotechnol. **10**, 129 (2015).

[26] I. Lovchinsky, J. D. Sanchez-Yamagishi, E. K. Urbach, S. Choi, S. Fang, T. I. Andersen, K. Watanabe, T. Taniguchi, A. Bylinskii, E. Kaxiras, P. Kim, H. Park, and M. D. Lukin, *Magnetic Resonance Spectroscopy of an Atomically Thin Material Using a Single-Spin Qubit*, Science **355**, 503 (2017).

[27] K. C. Nowack, E. M. Spanton, M. Baenninger, M. König, J. R. Kirtley, B. Kalisky, C. Ames, P. Leubner, C. Brüne, H. Buhmann, L. W. Molenkamp, D. Goldhaber-Gordon, and K. A. Moler, *Imaging Currents in HgTe Quantum Wells in the Quantum Spin Hall Regime*, Nat. Mater. **12**, 787 (2013).

[28] Y. Anahory, J. Reiner, L. Embon, D. Halbertal, A. Yakovenko, Y. Myasoedov, M. L. Rappaport, M. E. Huber, and E. Zeldov, *Three-Junction SQUID-on-Tip with Tunable In-Plane and Out-of-Plane Magnetic Field Sensitivity*, Nano Lett. **14**, 6481 (2014).

[29] See Supplemental Material at http://link.aps.org/supplemental/10.1103/PhysRevX.10.011003 for a detailed discussion of the experimental details, data analysis and modeling, control experiments, and proposal for ultrafast photocurrent detection.

[30] K. Kang, K.-H. Lee, Y. Han, H. Gao, S. Xie, D. A. Muller, and J. Park, *Layer-by-Layer Assembly of Two-Dimensional Materials into Wafer-Scale Heterostructures*, Nature (London) **550**, 229 (2017).

[31] J. J. Bae, H. Y. Jeong, G. H. Han, J. Kim, H. Kim, M. S. Kim, B. H. Moon, S. C. Lim, and Y. H. Lee, *Thickness-Dependent In-Plane Thermal Conductivity of Suspended* MoS_2 *Grown by Chemical Vapor Deposition*, Nanoscale **9**, 2541 (2017).

[32] M. Kern, J. Jeske, D. W. M. Lau, A. D. Greentree, F. Jelezko, and J. Twamley, *Optical Cryocooling of Diamond*, Phys. Rev. B **95**, 235306 (2017).

[33] G. D. Fuchs, A. L. Falk, V. V. Dobrovitski, and D. D. Awschalom, *Spin Coherence during Optical Excitation of a Single Nitrogen-Vacancy Center in Diamond*, Phys. Rev. Lett. **108**, 157602 (2012).

[34] M. Yarali, X. Wu, T. Gupta, D. Ghoshal, L. Xie, Z. Zhu, H. Brahmi, J. Bao, S. Chen, T. Luo, N. Koratkar, and A. Mavrokefalos, *Effects of Defects on the Temperature-Dependent Thermal Conductivity of Suspended Monolayer Molybdenum Disulfide Grown by Chemical Vapor Deposition*, Adv. Funct. Mater. **27**, 1704357 (2017).

[35] Z.-Y. Ong, Y. Cai, and G. Zhang, *Theory of Substrate-Directed Heat Dissipation for Single-Layer Graphene and Other Two-Dimensional Crystals*, Phys. Rev. B **94**, 165427 (2016).

[36] Y. Romach, C. Müller, T. Unden, L. J. Rogers, T. Isoda, K. M. Itoh, M. Markham, A. Stacey, J. Meijer, S. Pezzagna, B. Naydenov, L. P. McGuinness, N. Bar-Gill, and F. Jelezko, *Spectroscopy of Surface-Induced Noise Using Shallow Spins in Diamond*, Phys. Rev. Lett. **114**, 017601 (2015).

[37] J. Su, Z. Liu, L. Feng, and N. Li, *Effect of Temperature on Thermal Properties of Monolayer* MoS_2 *Sheet*, J. Alloys Compd. **622**, 777 (2015).

[38] D. Saha and S. Mahapatra, *Analytical Insight into the Lattice Thermal Conductivity and Heat Capacity of Monolayer* MoS_2, Physica (Amsterdam) **83E**, 455 (2016).

[39] J. Hone, B. Batlogg, Z. Benes, A. T. Johnson, and J. E. Fischer, *Quantized Phonon Spectrum of Single-Wall Carbon Nanotubes*, Science **289**, 1730 (2000).

[40] J. C. Lasjaunias, K. Biljaković, Z. Benes, J. E. Fischer, and P. Monceau, *Low-Temperature Specific Heat of Single-Wall Carbon Nanotubes*, Phys. Rev. B **65**, 113409 (2002).

[41] J. Karch, C. Drexler, P. Olbrich, M. Fehrenbacher, M. Hirmer, M. M. Glazov, S. A. Tarasenko, E. L. Ivchenko, B. Birkner, J. Eroms, D. Weiss, R. Yakimova, S. Lara-Avila, S. Kubatkin, M. Ostler, T. Seyller, and S. D. Ganichev, *Terahertz Radiation Driven Chiral Edge Currents in Graphene*, Phys. Rev. Lett. **107**, 276601 (2011).

[42] D. Sun, C. Divin, J. Rioux, J. E. Sipe, C. Berger, W. A. De Heer, P. N. First, and T. B. Norris, *Coherent Control of Ballistic Photocurrents in Multilayer Epitaxial Graphene Using Quantum Interference*, Nano Lett. **10**, 1293 (2010).

[43] S. A. Momenzadeh, R. J. Stöhr, F. F. de Oliveira, A. Brunner, A. Denisenko, S. Yang, F. Reinhard, and J. Wrachtrup, *Nanoengineered Diamond Waveguide as a Robust Bright Platform for Nanomagnetometry Using Shallow Nitrogen Vacancy Centers*, Nano Lett. **15**, 165 (2015).

[44] P. Kehayias, A. Jarmola, N. Mosavian, I. Fescenko, F. M. Benito, A. Laraoui, J. Smits, L. Bougas, D. Budker, A. Neumann, S. R. J. Brueck, and V. M. Acosta, *Solution Nuclear Magnetic Resonance Spectroscopy on a Nanostructured Diamond Chip*, Nat. Commun. **8**, 188 (2017).

[45] G. Balasubramanian, P. Neumann, D. Twitchen, M. Markham, R. Kolesov, N. Mizuochi, J. Isoya, J. Achard, J. Beck, J. Tissler, V. Jacques, P. R. Hemmer, F. Jelezko, and J. Wrachtrup, *Ultralong Spin Coherence Time in Isotopically Engineered Diamond*, Nat. Mater. **8**, 383 (2009).

[46] A. Brenneis, L. Gaudreau, M. Seifert, H. Karl, M. S. Brandt, H. Huebl, J. A. Garrido, F. H. L. Koppens, and A. W. Holleitner, *Ultrafast Electronic Readout of Diamond Nitrogen–Vacancy Centres Coupled to Graphene*, Nat. Nanotechnol. **10**, 135 (2015).

[47] K. J. Tielrooij, L. Orona, A. Ferrier, M. Badioli, G. Navickaite, S. Coop, S. Nanot, B. Kalinic, T. Cesca, L. Gaudreau, Q. Ma, A. Centeno, A. Pesquera, A. Zurutuza, H. De Riedmatten, P. Goldner, F. J. G. De Abajo, P. Jarillo-Herrero, and F. H. L. Koppens, *Electrical Control of Optical Emitter Relaxation Pathways Enabled by Graphene*, Nat. Phys. **11**, 281 (2015).

[48] L. Thiel, Z. Wang, M. A. Tschudin, D. Rohner, I. Gutiérrez-Lezama, N. Ubrig, M. Gibertini, E. Giannini, A. F. Morpurgo, and P. Maletinsky, *Probing Magnetism in 2D Materials at the Nanoscale with Single-Spin Microscopy*, Science **364**, 973 (2019).

[49] R. Yan, J. R. Simpson, S. Bertolazzi, J. Brivio, M. Watson, X. Wu, A. Kis, T. Luo, A. R. H. Walker, and H. G. Xing, *Thermal Conductivity of Monolayer Molybdenum Disulfide Obtained from Temperature-Dependent Raman Spectroscopy*, ACS Nano **8**, 986 (2014).

[50] T. Wolf, P. Neumann, K. Nakamura, H. Sumiya, T. Ohshima, J. Isoya, and J. Wrachtrup, *Subpicotesla Diamond Magnetometry*, Phys. Rev. X **5**, 041001 (2015).